Materials Advances

ROYAL SOCIETY OF CHEMISTRY

PAPER

View Article Online
View Journal | View Issue

Check for updates

Cite this: *Mater. Adv.*, 2025, **6**, 6052

Received 13th January 2025, Accepted 14th July 2025

DOI: 10.1039/d5ma00034c

rsc.li/materials-advances

Fabrication and characterization of high-tensile-strength PEO–PVP blend-based multifunctional composites for sodium-ion structural batteries†

Vasan Iyer, *[ab] Sandeep Kumar, [c] Håkan Pettersson, [de] Jan Petersen, [ab] Sebastian Geier [ab] and Peter Wierach [abf]

The structural integration of energy storage could play a pivotal role in designing more efficient, lightweight systems such as electric transport, internet of things (IoT) devices and autonomous systems. The current work focuses on the fabrication and characterization of novel multifunctional composites for sodium-ion structural batteries. A PEO–PVP polymer matrix with added InAs nanowires and glass fiber reinforcements was used to fabricate a structural electrolyte (GF_PEO–PVP–InAsNW–$NaPF_6$). It shows an ionic conductivity of 1.7×10^{-4} S cm^{-1} at 70 °C, an electrochemical stability window of 0 to 3.7 V, a sodium ion transference number of 0.40 and a high tensile strength of 76.5 MPa. A structural electrode is fabricated by laminating the electrolyte with intermediate modulus carbon fibers (CF) and it shows a high tensile strength of 171.5 MPa. The structural CF‖GF_PEO–PVP–InAsNW–$NaPF_6$‖Na cell provides a typical energy density of 17.5 Wh kg^{-1} at 0.1C rate and accomplished 600 cycles at 0.8C rate while retaining 80% capacity at the end of 280 cycles. The investigation in this preliminary work reveals addition of InAs nanowire fillers enhances both the tensile strength and ionic conductivity of the structural electrolyte and boosts the cycling stability of the structural cell by delaying sodium dendrite formation, and the usage of intermediate modulus carbon fibers in the fabricated electrodes demonstrates sodium-ion intercalation capabilities. The fabricated components display multifunctional performance and show good potential for sodium-ion structural battery applications.

Introduction

The electrification transition of the automobile industry is currently developing at a rapid pace, which is essential to meet the greenhouse gases emissions reduction demand by the year 2035 set by the European Union (EU) Green Deal.[1] The global transportation sector currently produces approximately 23% of the carbon dioxide (CO_2) emissions (as shown in Fig. 1a), in which the aviation sector contributes roughly 2.5%.[2] The impact of the aviation sector is high due to the CO_2 emissions in the upper regions of the earth's atmosphere. If the aviation sector is continued to be powered only by fossil fuels, without exploring alternative technologies or electrification, this will lead to an extreme scenario in which the aviation sector alone will be responsible for 50% of the global transport emissions (as shown in Fig. 1b).[2] To avoid such a scenario, it is necessary to integrate aviation in the process of electrification like other transportation sectors, which is a challenging task. Hence the deadline is set for 2050 for the aviation sector to achieve net-zero emissions.[3–5]

Lithium-ion batteries have established themselves as the key driver of electrification of electric road transport. In the aviation sector, the overall weight plays a crucial role and hence batteries with very high energy densities are required to achieve electrification. Some studies predict that battery technology will advance enough by the year 2030 to achieve a flight range of 700 miles and up to 1600 miles by the year 2040.[6] One important factor missing in these studies is the battery weight, which contributes to the overall vehicle weight and increases according to the vehicle range requirements. An interesting

---

[a] *Cluster of Excellence SE2A – Sustainable and Energy Efficient Aviation, Technische Universität Braunschweig, 38108, Braunschweig, Germany. E-mail: vasan.iyer@dlr.de, vasan.iyer@tu-clausthal.de*

[b] *Institute of Lightweight Systems, Department of Multifunctional Materials, German Aerospace Center (DLR), Lilienthalplatz 7, 38108, Braunschweig, Germany*

[c] *Center for Nanoscience and Nanotechnology, Jamia Millia Islamia, New Delhi, 110025, India*

[d] *School of Information Technology, Halmstad University, Box 823, SE-301 18 Halmstad, Sweden*

[e] *Solid State Physics and NanoLund, Lund University, Box 118, SE-221 00 Lund, Sweden*

[f] *Institute of Polymer Materials and Plastics Engineering, Technische Universität Clausthal, Agricolastrasse 6, Clausthal-Zellerfeld, 38678, Germany*

† Electronic supplementary information (ESI) available. See DOI: **https://doi.org/10.1039/d5ma00034c**

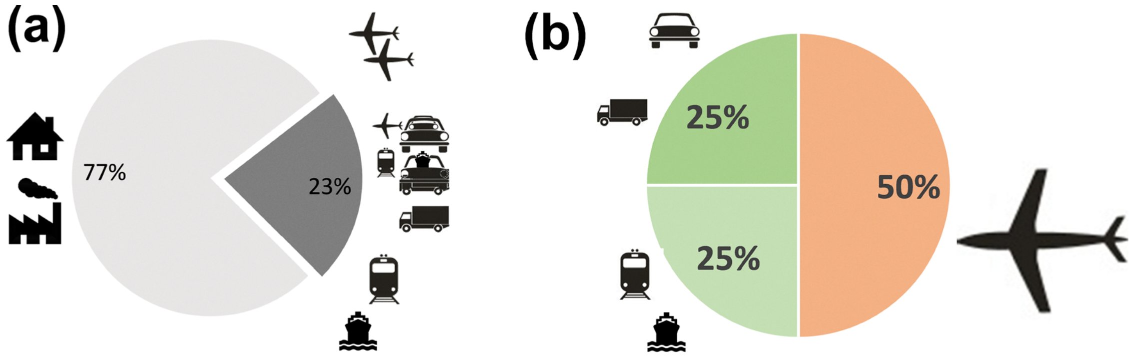

Fig. 1 (a) Overall CO_2 emissions breakdown in the current scenario. (b) CO_2 emissions breakdown in an extreme case scenario for the transportation sector in 2050. Reproduced with permission.[2] Copyright 2019, SE2A.

example is the Tesla model 3 car, which uses lithium-ion batteries that contribute to 18% (324 kg) of the overall car weight for its standard range (54 kWh) version, while the battery weight increases to almost 27% (480 kg) of the car weight for its long range (75 kWh) version.[7] Reducing the battery weight will improve the overall efficiency of the vehicle and increase its range capabilities.

In the current scenario, the batteries are completely isolated from the vehicle structure and hence contribute heavily to the overall mass of the vehicle (as depicted in Fig. 2a). The concept of integrating energy storage within the structures helps in achieving battery weight reduction, since the batteries are seen as a function rather than as a distinct component and hence they are referred to as structural batteries.[8] Depending upon the degree of integration (DOI), the batteries could be inserted strategically in the empty spaces within the structure (DOI I) or they can simply be attached to the surface of the structure by using thin film batteries or sandwiched inside laminated composites (DOI II).[9–12] The degree of integration could even reach a level where the batteries are identical to the structure (DOI III–IV).[13–15]

The complexity of structural batteries increases with higher DOI and true multifunctionalization is achieved with DOI III–IV type structural batteries. In this case, it has the capacity to provide massless energy storage, as the battery is now well integrated within the structure (as depicted in Fig. 2b). This could lead to lightweight systems with high overall efficiency and improved vehicle utility space. To design higher DOI type batteries, it is essential that each component in the battery architecture can perform multiple functions.

When compared to conventional batteries, the electrolyte in a structural battery should not only facilitate transfer of ions but also contribute to the structural strength. Similarly, the electrodes in a structural battery should be capable of both ion-storage and possess considerable mechanical strength. This makes it challenging to design structural batteries with higher DOI, wherein a great deal of optimization is required of both the mechanical and electrochemical properties of the battery components.[17–19]

The interesting properties of carbon fibers (CFs) make them an important component when it comes to fabricating higher DOI multifunctional structural batteries. CFs possess both the ability to store ions and function as electrodes and also to act as current collectors.[17,20–23] They also possess considerable mechanical strength making them a good multifunctional component for structural energy storage applications.[17,24,25] Another important consideration for designing structural batteries lies in the intercalation mechanism of ions into carbon fiber microstructures. Previous structural battery research was mainly based on lithium ion intercalation inside carbon fiber microstructures.[17,25,26] Lithium ions intercalate in-between the carbon fiber graphitic layers, and also have the ability to intercalate at the edges and lattice surfaces, while sodium ions intercalate inside pores or defect sites and in lattice surfaces of carbon fiber microstructures, such as those in hard carbon.[27–31] This calls for adopting new strategies while designing

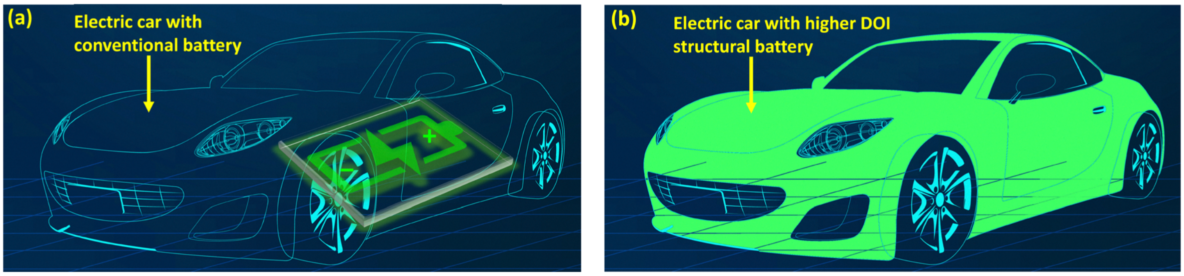

Fig. 2 (a) Image showing the system architecture of an electric car with a conventional battery. (b) Image showing the system architecture of an electric car with integrated structural batteries. Images adapted and reproduced with permission (image attribution: designed by Freepik).[16]

structural batteries based on sodium-ion intercalation inside CFs, which is the focus of the present work. Studies reported that the intermediate modulus (IM) type carbon fibers possess microstructures similar to hard carbons which favor sodium-ion intercalation, therefore the present work uses IM type carbon fibers for the fabrication of the structural cell.[20,28,31]

The polymer used as the matrix material is a key component in the structural battery architecture, as it plays the important role of an electrolyte, assisting in ion transport. The previous studies related to lithium-ion based DOI III structural batteries used polymers both as an electrolyte and as a binder material for the fibers, while some designs also explored structural battery designs using all solid-state polymer electrolytes.[22,26,32]

The present work focuses on sodium-ion based DOI III structural battery architectures using a solid-state polymer electrolyte based on a poly(ethylene oxide) (PEO)–poly(vinyl pyrrolidone) (PVP) blend polymer. Although PEO has a low glass transition temperature and offers good mechanical, thermal and electrochemical properties, its room temperature ionic conductivity is very low due to its crystalline nature.[33–36] The addition of inorganic active fillers or plasticizers to the PEO matrix is known to improve the ion transport capabilities by reducing the crystalline nature of the polymer.[37–39] In recent studies, multifunctional composites (structural electrolyte and structural electrode) for sodium-ion based structural battery applications were investigated using PEO as the matrix incorporated with active fillers. The first study involved the addition of NASICON type $Na_3Zr_2Si_2PO_{12}$ (NZSP) inorganic ceramic active nanoparticle fillers to the PEO matrix to fabricate multifunctional composites, while the second study used succinonitrile plasticizers as fillers to the PEO matrix.[40,41] In both studies, the fabricated structural cell showed good cycling stability and was able to retain 80% capacity at the end of 200 cycles.

In the present study, a different approach for the fabrication of multifunctional composites is investigated in which a PEO–PVP blend polymer was used. The choice of PVP to blend with PEO is due to its charge transport mechanism and amorphous content. The ion mobility in PVP is enhanced due to the presence of the rigid pyrrolidone group, and the side-chains containing the carbonyl (C═O) group support complex formation with inorganic salts.[42–44] Recent studies also showed that the addition of high-aspect-ratio nanowires (NWs) to the polymer matrix improved the ionic conductivity due to the NWs' ability to provide long pathways for ionic conduction.[45] Until now, the structural battery architecture mainly used inorganic nanoparticle fillers and plasticizers to the polymer matrix to enhance ionic conductivity. The main objective of the present study is to fabricate and investigate novel multifunctional composites based on a PEO–PVP polymer blend matrix incorporated with InAs nanowires for structural sodium-ion battery applications. Initially, the solid polymer electrolyte (SPE) was prepared by incorporating the InAs NWs into the PEO–PVP polymer blend using the solution-casting technique. The structural electrolyte was then fabricated by reinforcing the SPE with glass fiber. The structural electrode was fabricated by laminating the IM type carbon fibers with the structural electrolyte. The fabricated composites are then investigated for electrochemical, mechanical and thermal performance, along with the structural cell performance, and the results obtained are reported and discussed in the subsequent sections.

Experimental section

Chemicals and materials

All chemicals were purchased from Sigma-Aldrich and Alfa Aesar GmbH. Glass fiber woven fabric and spread tow carbon fibers were purchased from R&G Faserverbundwerkstoffe GmbH, Waldenbuch, Germany. Two-sided siliconized paper for heat pressing was obtained from Laufenberg GmbH, Krefeld, Germany. Complete details about the materials are available in the ESI.†

Synthesis of InAs nanowires

Single-crystalline InAs NWs with an average diameter of ~40 nm were synthesized by a low-temperature solvothermal method.[46] The synthesis is detailed in the ESI.†

Preparation of solid polymer electrolytes

The solid polymer electrolyte was prepared as shown in the schematic (step 1) in Fig. 3. A precursor solution was made by mixing the polymers poly(ethylene oxide) (PEO) and poly(vinyl pyrrolidone) (PVP) in methanol solvent. The concentration ratio of the PEO–PVP blend was kept constant as 80 : 20. Initially, 0.4 g of PEO was blended with 0.1 g of PVP using methanol as the solvent. Then, 0.15 g of $NaPF_6$ was added to the solution in such a way that the stoichiometry ratio of $(\ddot{O}:Na^+)$ was maintained at 8 : 1. The container was sealed and stirred for 2 hours until all the salt and the polymer blend were dissolved. Then various amounts of the prepared InAs nanowires ranging from 0 to 3.0 wt% were added to the mixture, and then sonicated (using Branson 250 Digital Sonifier, Branson Ultrasonics, Dietzenbach, Germany) with a pulsed 10% amplitude for 30 minutes to avoid agglomeration of the nanowire fillers. The mixture was again stirred continuously for 6 hours until a homogenous mixture was obtained. Finally, the mixture was cast into a PTFE dish and kept aside in the fume-hood for 6 hours until a uniform membrane was formed and the solvent had evaporated. To ensure complete elimination of the methanol solvent, the membranes were vacuum dried using a desiccator at 40 °C for 24 hours. Finally, solid polymer electrolyte (SPE) membranes with a thickness of 120 μm were obtained.

Preparation of multifunctional composites (structural electrolyte and structural electrode)

The GF_PEO–PVP–InAsNW–$NaPF_6$ structural electrolytes were synthesized by reinforcing glass fibers in between two thin solid polymer electrolyte layers (as shown in Fig. 3 (step 2)) and

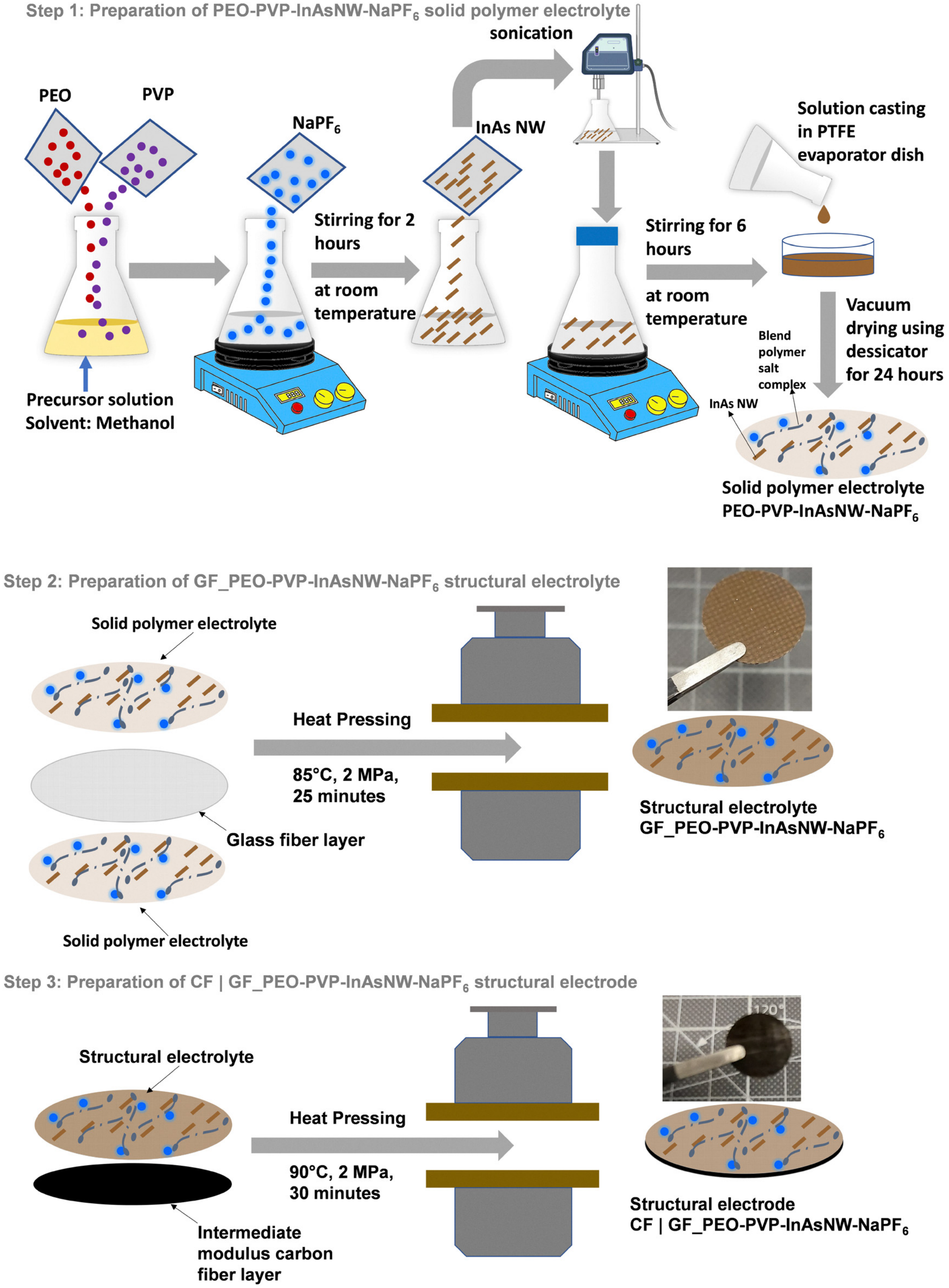

Fig. 3 Schematic showing the synthesis of InAs nanowire-filled solid polymer electrolyte and multifunctional composites (structural electrolyte and structural electrode).

then heat pressing using Collins P500S press, (COLLIN Lab & Pilot Solutions GmbH, Maitenbeth, Germany) at 85 °C, 2 MPa for 25 minutes. The thickness of the structural electrolyte was measured to be 340 μm.

The obtained structural electrolyte (GF_PEO–PVP–InAsNW–$NaPF_6$) was placed over an intermediate modulus carbon fiber layer as shown in Fig. 3 (step 3), and then it was heat pressed (using Collins P500S press, COLLIN Lab & Pilot Solutions

GmbH, Maitenbeth, Germany) at 90 °C, 2 MPa for 30 minutes to obtain the structural electrode (CF|GF_PEO–PVP–InAsNW–$NaPF_6$) with a thickness of 390 μm.

Characterization

The characterization and morphology study of the InAs nanowires (NWs), the SPE, structural electrolyte and structural electrode were performed using scanning electron microscopy (SEM) (FEI, Thermo Fisher Scientific Inc., Dreieich, Germany) and energy dispersive X-ray analysis (EDAX) techniques.

The ionic conductivities of the prepared electrolytes were assessed using electrochemical impedance spectroscopy (EIS). The cells were made with stainless steel (SS) blocking electrodes in the form SS‖electrolyte‖SS and the EIS spectra were recorded using the potentiostat Reference 3000 (Gamry LCC, Warminster, PA, USA) in the frequency range 1 Hz to 10^6 Hz, with an applied AC potential of 10 mV.

Symmetrical cells with the Na‖electrolyte‖Na (Fig. S2, ESI†) configuration were used to assess the sodium ion transference numbers of the prepared electrolyte from the AC–DC (alternating current–direct current) experiments. The EIS spectrum was initially recorded in the frequency range from 1 Hz to 1 MHz with an AC perturbation voltage of 10 mV. Then, the chronoamperogram or current evolution is recorded for an applied DC perturbation voltage of 10 mV until the current reached a steady state. Again, the EIS spectrum is recorded with a 10 mV AC perturbation voltage, and the resistances were calculated from the obtained Nyquist plots before and after the application of dc polarization.[47]

Asymmetrical cells with the SS‖electrolyte‖Na (Fig. S2, ESI†) configuration were used to analyze the electrochemical stability window (ESW) of the fabricated electrolytes by linear sweep voltammetry (LSV). The LSV is carried out by doing a voltage scan from 0 V to 6 V, using a scan rate of 1 mV s^{-1} at 70 °C.

The mechanical strength of the prepared solid polymer electrolytes was analyzed by tensile testing using a 10 N load cell. For the multifunctional components (structural electrolyte and structural electrode), a 5 kN load cell was used. All the samples were prepared in accordance with the ASTM D-638 Type V standard.[48] The tensile tests were performed in the universal testing machine (UTM) (using Zwick GmbH & Co. KG, Ulm, Germany) with a loading rate set at 2 mm min^{-1}, and a high-end 3D industrial camera (ZEISS ARAMIS 3D, Carl Zeiss IQS GmbH, Oberkochen, Germany) was used for contactless and precise strain measurements (as shown in Fig. S3, ESI†). The structural electrolyte and the structural electrode sample surfaces were coated with powder to pixelate the samples for precise strain measurements.

Structural sodium cell preparation and testing

The structural sodium cell CF‖GF_PEO–PVP–InAsNW–$NaPF_6$‖Na was prepared in the 2032-coin cell configuration, where the carbon fiber part of the fabricated structural electrode material acts as the cathode and pure sodium metal as the anode. The structural cathode cut into a disc shape (with a diameter of 10 mm) was placed above the prepared sodium metal foil in a disc shape (with a diameter of 14 mm) with the electrolyte part facing the sodium foil as shown in Fig. S4 (ESI†). The coin cell was assembled inside the glove box in an argon environment (with humidity 0 ppm and oxygen 0 ppm) using the MTI MSK-160E pressure adjustable electric crimper (manufactured by MTI Corporation, California, USA). The performance of the fabricated structural cell was analyzed using a Reference 3000 potentiostat (Gamry LCC, Warminster, PA, USA) connected to the coin cell holder (Part number: 992-00159, Gamry LCC, Warminster, PA, USA). The cell capacities were estimated based on the aerial weight of the carbon fiber electrode.

Results and discussion

Characterization of InAs nanowires, structural electrolyte and structural electrode

The NWs due to their linear structure can offer a directed pathway for ionic transport, allowing for faster ion conduction along the nanowire axis. It is observed that the negatively-charged surface of the InAs NWs in the SPEs both promotes dissociation of contact ion-pairs, and provides a fast pathway for Na^+ diffusion *via* hopping from one negatively charged site to the next, leading to increased ion mobility.[49] Thus, InAs NW-filled SPEs show a drastic conductivity enhancement mainly due to the formation of a hitherto unrevealed fast-conductive network induced by the unique NW surface morphology.

The synthesis of InAs NWs is described in the Experimental Section, where the NWs are obtained using a low temperature solvothermal method. The final combined mixture obtained after the reaction (involving reactants $InCl_3{\cdot}4H_2O$ and As_2O_3) was sonicated and centrifuged, and the final product is vacuum dried to obtain high quality InAs NWs. Fig. 4a shows the scanning electron microscopy (SEM) images of the InAs NW network with ∼40 nm diameter and length >1 μm. The single-phase nature of the synthesized InAs NWs was confirmed by X-ray diffraction (XRD) data as shown in Fig. S5 (ESI†). The HRTEM image (Fig. 4b) shows a single strand of InAs NWs with few stacking faults and confirms the high quality zinc blende (ZB) crystal structure.

The preparation of solid polymer electrolyte is elaborated in the Experimental Section. When the polymers PEO and PVP are mixed in the methanol solvent, they form a blend polymer matrix as illustrated in Fig. 5. When the $NaPF_6$ salt is added (with a stoichiometric ratio ($\ddot{O}:Na^+$) of 8 : 1) to the mixture and stirred, the salt is dissociated, and a blend polymer salt complex is formed (as shown in Fig. 5). The carbonyl group ($C{=}O$) in the PVP side-chains forms complexes with PEO and inorganic salts. The stoichiometric ratio ($\ddot{O}:Na^+$) of 8 : 1 was studied to give the best ionic conductivity.[44]

The structural electrolyte (SE) was prepared by sandwiching a layer of woven glass fiber (GF) fabric in between two thin SPE and the SEM image of the SE surface is shown in Fig. S6 (ESI†), which shows uniform distribution of InAs NWs without much agglomeration, which is crucial for the performance of the

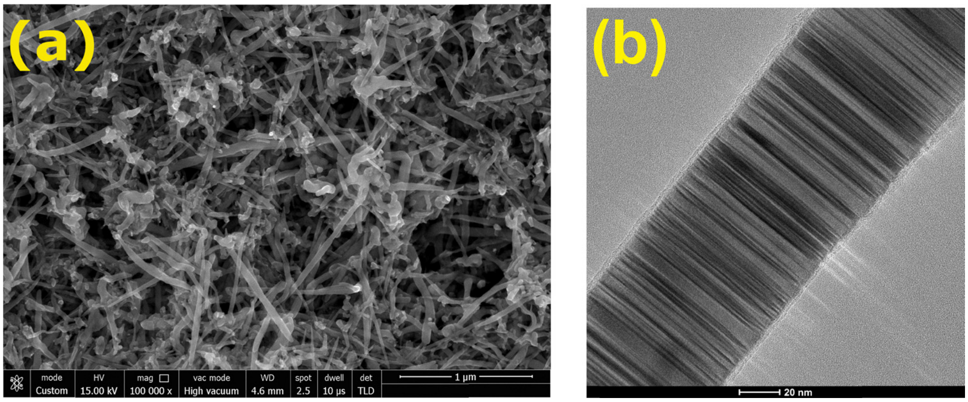

Fig. 4 (a) Scanning electron microscopy image of an InAs nanowire network. (b) HRTEM image showing a single strand of InAs nanowires.

structural electrolyte and the structural cell. The cross-section of the SE is shown in Fig. 6a, where the GF reinforcements in between the two SPE layers can be seen, and it is designated as GF_PEO–PVP–InAsNW–$NaPF_6$.

Similarly, Fig. 6b displays the cross-sectional view of the fabricated structural electrode (CF|GF_PEO–PVP–InAsNW–$NaPF_6$), where the distinct SE layer and the CF layer are marked. Energy dispersive X-ray analysis (EDAX) was performed on the surface of the SE, and the chemical constituents of SE are shown in the EDAX pattern (Fig. S7, ESI†). Fig. S7 (ESI†) displays the SEM-EDAX mapping, where the chemical composition present in the sample can be seen, the presence of indium (In) and arsenic (As) confirms the presence of nanowire fillers. To study the distinction, the electrolytes PEO–PVP–$NaPF_6$ and GF_PEO–PVP–$NaPF_6$ are also prepared without nanowire fillers. The fabricated electrolytes and electrode are shown in Fig. S8 (ESI†).

Electrochemical characterization

The structural electrolyte should possess good ion transference, ionic conductivity, sodium dendrite growth inhibition capability and cycling stability for structural battery applications. Hence, these properties are evaluated using the various electrochemical characterization techniques described in Section 2. For comparison, the other prepared electrolytes are also evaluated for these critical parameters.

The ionic conductivities of the various prepared electrolytes were assessed using the EIS technique, where the EIS spectrum was recorded in the frequency range 1 Hz to 1 MHz and the ionic conductivity (σ) was calculated using the bulk resistance (R_B) values obtained from the Nyquist plots using eqn (1) with electrolyte thickness (t) and geometrical area (A) in contact with the blocking stainless steel electrodes of the cell.

$$\sigma = \frac{t}{AR_B} \tag{1}$$

The bulk resistance (R_B) can be evaluated using the EIS equivalent circuit (Fig. S9, ESI†) or directly from the recorded EIS spectrum, where the Nyquist plot intercepts the x axis (real axis).

A comparison of SPE with various wt% of InAs NW fillers is shown in Fig. S10 (ESI†). The addition of InAs NWs to the PEO–PVP matrix enhanced the ionic conductivity, particularly the SPE containing 1.0 wt% InAs NW fillers showed the maximum ionic conductivity. Therefore, the multifunctional matrix composite or the structural electrolyte (GF_PEO–PVP–InAsNW–$NaPF_6$) for the present work is fabricated with SPE containing 1.0 wt% InAs NW fillers to ensure better battery performance.

Fig. 7a shows the Nyquist plots of the various prepared electrolytes at 40 °C. The SPE PEO–PVP–InAsNW–$NaPF_6$ with 1.0 wt% InAs NW fillers showed an ionic conductivity of 1.07×10^{-4} S cm^{-1} while the SPE without nanowire fillers (PEO–PVP–$NaPF_6$) showed an ionic conductivity of 2.6×10^{-6} S cm^{-1}. The glass fiber embedded structural electrolytes GF_PEO–PVP–InAsNW–$NaPF_6$ and GF_PEO–PVP–$NaPF_6$ displayed ionic conductivities of 7.3×10^{-6} S cm^{-1} and 1.3×10^{-6} S cm^{-1}, respectively. The low ionic conductivities are due to the insulative glass fibers reinforced between the SPE for enhancing mechanical strength.[32,40]

Fig. 7b shows the EIS spectra of the structural electrolyte (GF_PEO–PVP–InAsNW–$NaPF_6$) at different temperatures and it displayed an ionic conductivity of 1.7×10^{-4} S cm^{-1} at 70 °C, suitable for battery operation. Fig. 7c shows the Arrhenius plots

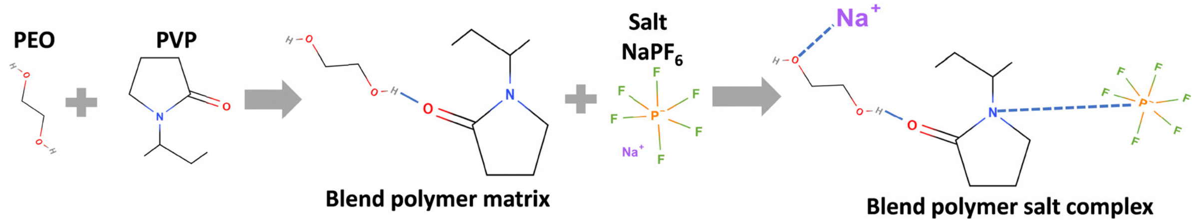

Fig. 5 Schematic showing the polymer blend matrix formation and the interaction mechanism in the blend polymer salt complex.

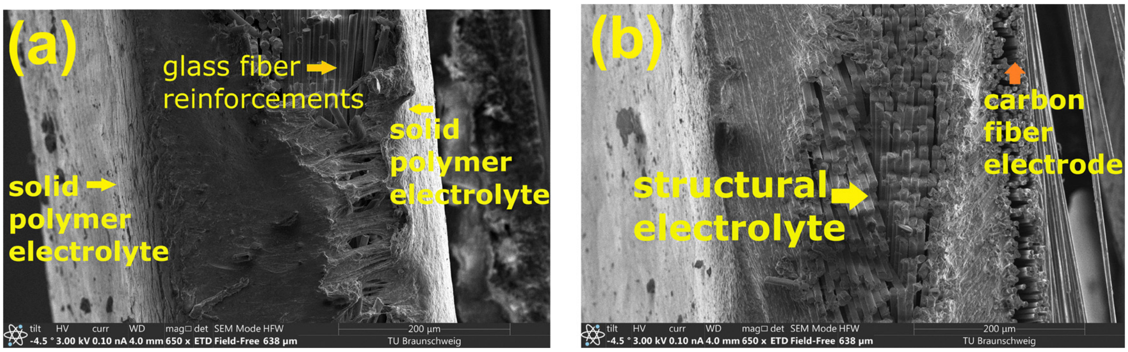

Fig. 6 SEM images: (a) cross sectional view of the structural electrolyte showing glass fibers sandwiched between two solid polymer electrolyte membranes. (b) Cross-sectional view of the structural electrode CF|GF_PEO–PVP–InAsNW–$NaPF_6$ showing the carbon fiber electrode adjacent to the structural electrolyte.

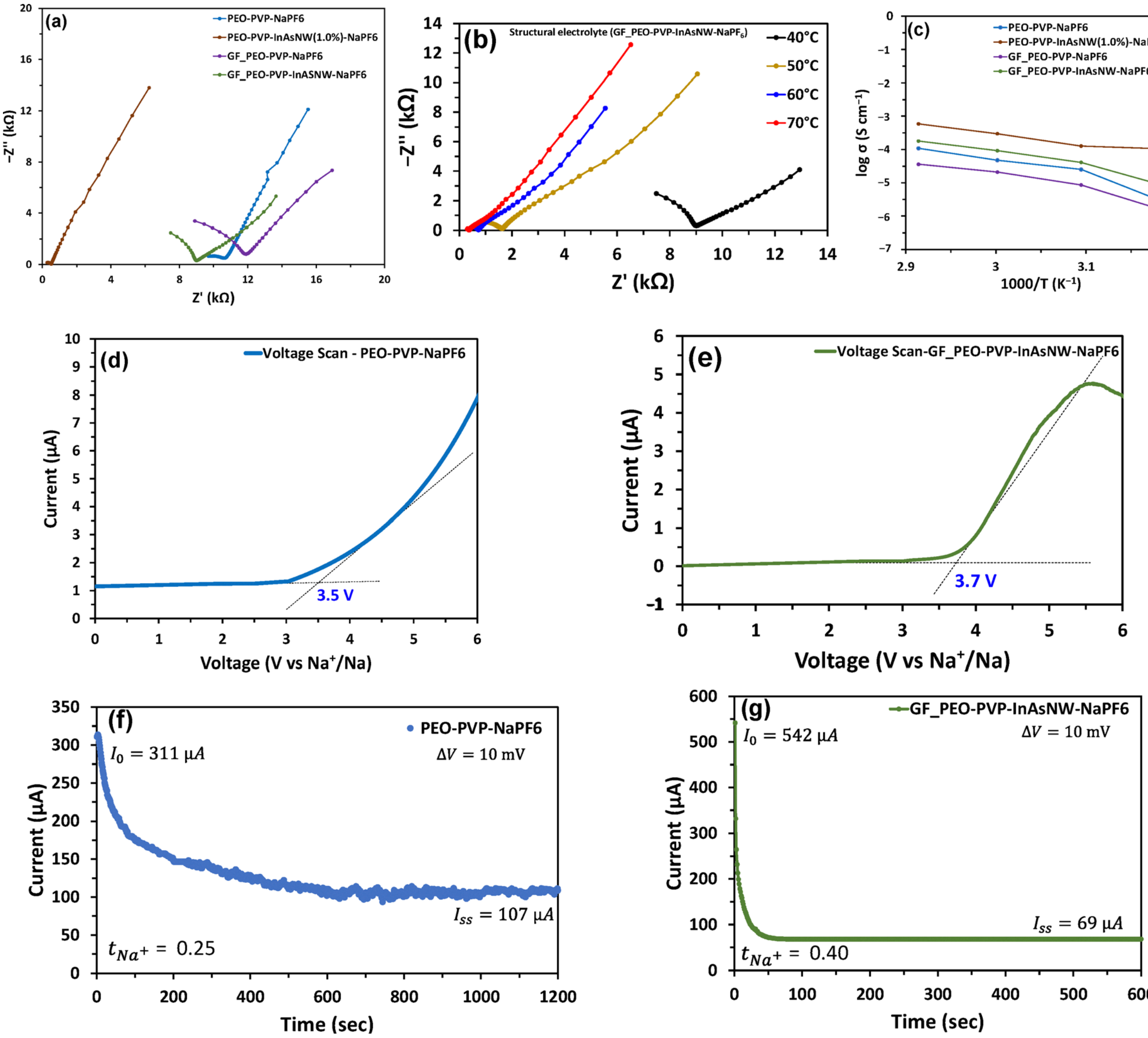

Fig. 7 Electrochemical characterization: (a) EIS of different electrolytes at 40 °C. (b) EIS of the structural electrolyte (GF_PEO–PVP–InAsNW–$NaPF_6$) at different temperatures. (c) Arrhenius plots of various electrolytes. (d) Linear sweep voltammetry (LSV) curve of the PEO–PVP–$NaPF_6$ electrolyte. (e) Linear sweep voltammetry (LSV) curve of the structural electrolyte GF_PEO–PVP–InAsNW–$NaPF_6$. (f) Chronoamperogram or current response of the Na‖PEO–PVP–$NaPF_6$‖Na symmetrical cell to the applied dc polarization. (g) Chronoamperogram or current response and EIS of the Na‖GF_PEO–PVP–InAsNW–$NaPF_6$‖Na symmetrical cell to the applied dc polarization.

of the various prepared electrolytes, clearly showing the impact of InAs NW addition to the blend polymer matrix. Fig. S11 (ESI†) shows the variation in ionic conductivity values of all the prepared electrolytes at different temperatures.

As described in Section 2, the ESW is assessed using asymmetrical cells in the SS‖Electrolyte‖Na configuration. The linear sweep voltammetry (LSV) curves of the electrolytes PEO–PVP–$NaPF_6$ and GF_PEO–PVP–InAsNW–$NaPF_6$ obtained by performing a voltage scan from 0 V to 6 V with a scan rate of 1 mV s^{-1} at 70 °C are displayed in Fig. 7d and e, respectively. The SPE (PEO–PVP–$NaPF_6$) displayed an ESW of 3.5 V, while the structural electrolyte (GF_PEO–PVP–InAsNW–$NaPF_6$) showed an ESW of 3.7 V. The slight increase in the stability window could be attributed to the addition of glass fibers.[50]

The sodium-ion transference number of the electrolytes was determined by AC–DC experiments using symmetrical cells (Na‖electrolyte‖Na) as described in Section 2. Fig. S12 (ESI†) shows the EIS spectra recorded before and after the dc polarization. Fig. 7f and g display the recorded current response of Na‖PEO–PVP–$NaPF_6$‖Na and Na‖GF_PEO–PVP–InAsNW–$NaPF_6$‖Na cells, respectively, for the applied dc polarization voltage. The ion transference number was calculated using eqn (2), with the dc polarization voltage (ΔV) set to 10 mV.[47]

$$t_{\mathrm{Na}^+} = \frac{I_{\mathrm{ss}}(\Delta V - I_0 R_0)}{I_0(\Delta V - I_{\mathrm{ss}} R_{\mathrm{ss}})} \tag{2}$$

where the initial current (I_0) and steady state current (I_{ss}) values were obtained from the current response plots, and the initial resistance (R_0) and steady state charge transfer resistance (R_{ss}) were obtained from the EIS equivalent circuit model (Fig. S9, ESI†). The estimated sodium-ion transference numbers (Table S1, ESI†) of SPE (PEO–PVP–$NaPF_6$) and the structural electrolyte (GF_PEO–PVP–InAsNW–$NaPF_6$) are 0.25 and 0.40 at 70 °C respectively. The high ion transference number for the structural electrolyte clearly shows high sodium-ion mobility due

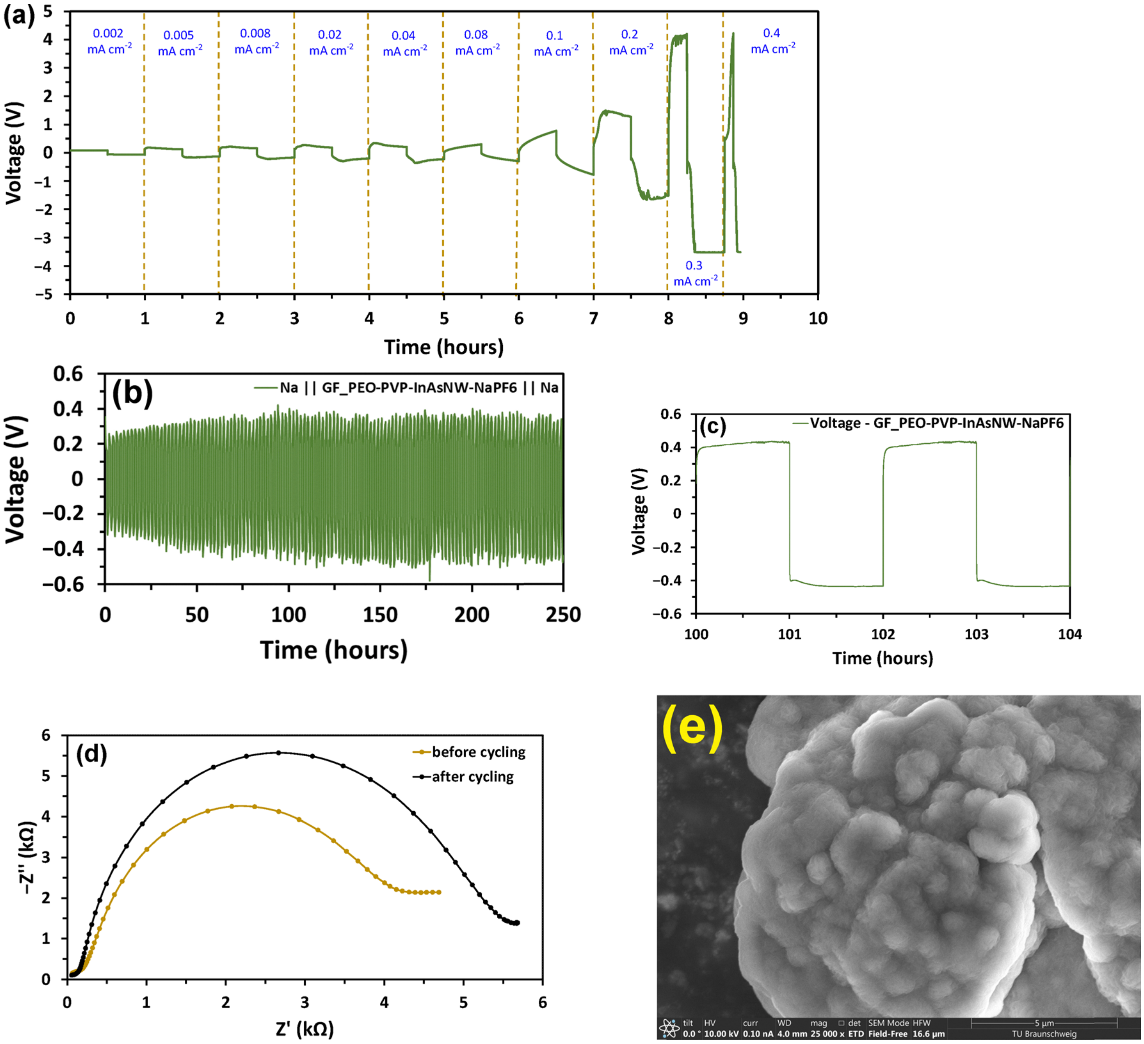

Fig. 8 Galvanostatic experiments for symmetric cell Na‖GF_PEO–PVP–InAsNW–$NaPF_6$‖Na at 70 °C: (a) critical charge density experiment plot showing galvanostatic cycling curves with varying current density. (b) Galvanostatic cycling at a current density of 0.08 mA cm^{-2}. (c) Typical voltage profile of the cell from 100 to 104 hours. (d) EIS of the cell before and after cycling. (e) SEM image of the Na electrode of the cell after cycling.

to the addition of InAs NWs and glass fiber reinforcements to the blend polymer matrix.[32]

The symmetrical cell (Na‖GF_PEO–PVP–InAsNW–NaPF$_6$‖Na) was galvanostatically cycled with varying current densities to determine the critical charge density (CCD) of the structural electrolyte and hence to assess its dendrite inhibition capacity. Fig. 8a shows the galvanostatic cycling curves, wherein each cycle was charged and discharged for 0.5 hours for an applied current density. Around 0.2 mA cm^{-2} the short circuiting of the cell slowly starts to appear, and the cell fails to charge continuously for 0.3 mA cm^{-2}, which clearly indicates that the sodium dendrites had percolated through the structural electrolyte material effectively short circuiting the cell.

Beyond the current density of 0.3 mA cm^{-2}, the cell fails to charge and immediately breaks down to 0 V indicating that the cell is destroyed due to short circuiting and the failure of dendrite inhibition capacity of the structural electrolyte. Therefore, the CCD of the structural electrolyte is determined to be 0.3 mA cm^{-2}.

The cycling stability of the structural electrolyte was assessed by galvanostatic cycling of the Na‖GF_PEO–PVP–InAsNW–NaPF$_6$‖Na cell for a constant current density of 0.08 mA cm^{-2}. The cell was charged for 250 hours as shown in Fig. 8b, and the voltage profile between 100 and 104 hours is shown in Fig. 8c. The cycling stability displayed by the structural electrolyte can be credited to the ability of InAs NW fillers to suppress sodium dendrite formation as confirmed by previous studies involving PEO based polymers with active fillers.[40] The charge transfer resistance after cycling is higher than before cycling as evident from the EIS spectra shown in Fig. 8d, which could be due to the inevitable sodium dendrite formation.[51,52] Fig. 8e displays the SEM image of the Na electrodes after cycling.

Mechanical characterization and thermal stability performance

In addition to ion transport and ion storage, the components of the structural cell should also be evaluated for load bearing capabilities. For this purpose, tensile tests were conducted as detailed in Section 2. The samples for tensile testing were prepared according to the ASTM D-638 Type V standard as shown in Fig. S13 (ESI†), and are tested using the UTM (Zwick GmbH & Co. KG, Ulm, Germany).

The SPE samples were evaluated using a 10 N load cell and the starting points of the tensile test for the PEO–PVP–NaPF$_6$ and PEO–PVP–InAsNW–NaPF$_6$ samples are shown in Fig. 9a and c, respectively. Both SPEs showed considerable elastic behavior and the maximum tensile strength of the PEO–PVP–NaPF$_6$ electrolyte is found to be 4.5 MPa (Fig. 9b) and that of PEO–PVP–InAsNW–NaPF$_6$ is 6.1 MPa (Fig. 9d). This is significantly higher than the values reported in a previous study using active NZSP nanoparticle fillers with PEO as the matrix material.[40] The increase in tensile strength in the present study can be attributed to the combined effect of the PEO–PVP blend polymer matrix and addition of InAs NWs. The value comparisons are shown in Table S2 (ESI†).

The experimental setup for the structural electrolyte (GF_PEO–PVP–InAsNW–NaPF$_6$) and structural electrode (CF|GF_PEO–PVP–InAsNW–NaPF$_6$) is shown in Fig. 10a and c,

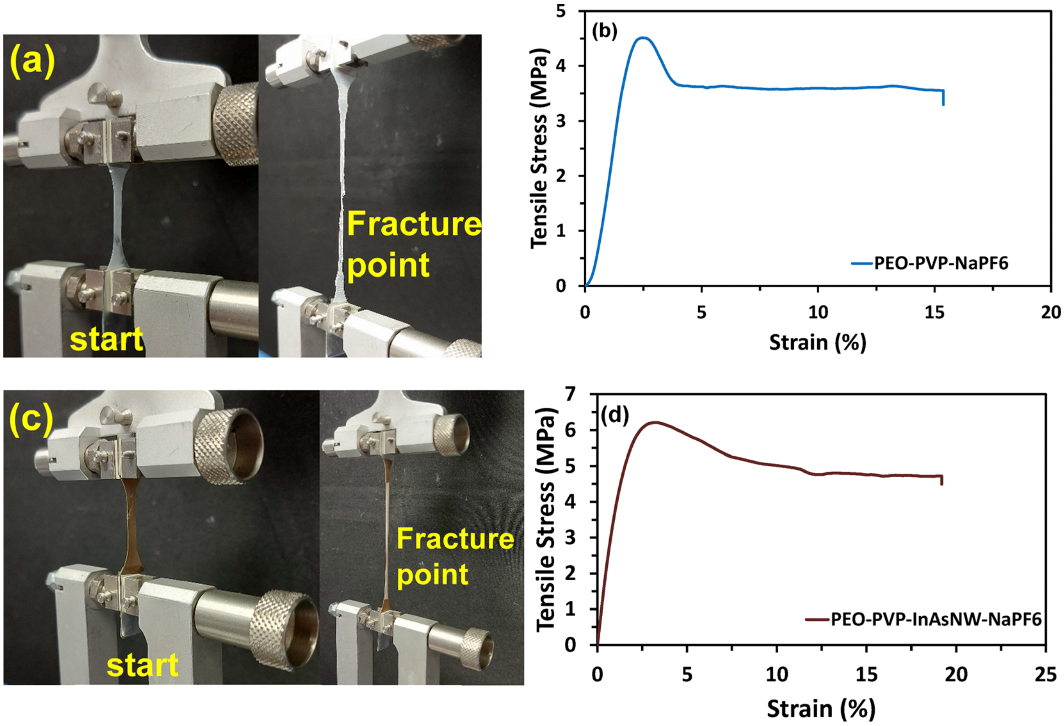

Fig. 9 Mechanical characterization of the solid polymer electrolyte: (a) experimental setup for the tensile test of PEO–PVP–NaPF$_6$. (b) Typical stress–strain curve of PEO–PVP–NaPF$_6$. (c) Experimental setup for the tensile test of PEO–PVP–InAsNW–NaPF$_6$. (d) Typical stress–strain curve of PEO–PVP–InAsNW–NaPF$_6$.

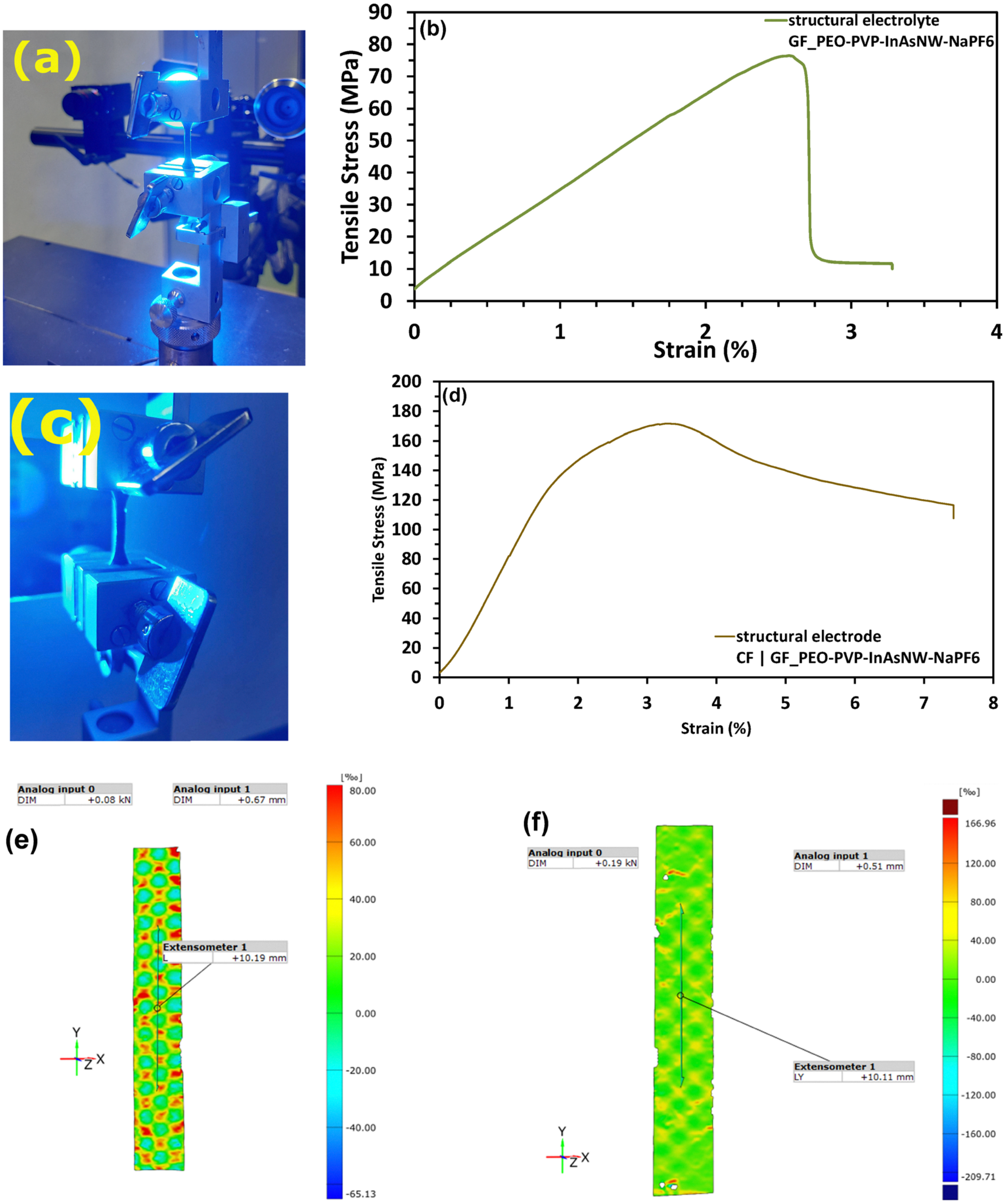

Fig. 10 Mechanical characterization: (a) experimental setup for the tensile test of structural electrolytes. (b) Typical stress–strain curve of the structural electrolyte GF_PEO–PVP–InAsNW–NaPF$_6$. (c) Experimental setup for the tensile test of structural electrodes. (d) Typical stress–strain curve of structural electrode CF|GF_PEO–PVP–InAsNW–NaPF$_6$. (e) Strain measurements for the structural electrolyte. (f) Strain measurements for the structural electrode.

respectively, and the tensile strength was evaluated with the help of a 5 kN load cell. From the typical stress–strain curves, the maximum tensile strength of the structural electrolyte and structural electrode was found to be 76.5 MPa (Fig. 10b) and 171.5 MPa (Fig. 10d), respectively.

When compared with SPE with NWs, the structural electrolyte showed nearly 13 times more tensile strength, due to glass fiber reinforcements. A similar high tensile strength can be seen in the structural electrode which is laminated with intermediate modulus carbon fibers. In comparison to the previous studies of multifunctional composites with polymer matrices incorporated with active NZSP nanoparticle fillers, and succinonitrile plasticizers, the structural strength displayed by both the structural electrolyte and structural electrode with InAs NW fillers in the present study is higher, and it is summarized in Fig. S14 (ESI†).[40,41]

This can be attributed mainly to high tensile strength of the SPE and to a certain extent to the small thickness of the prepared composites effectively reducing the cross-sectional area. The samples captured during the tensile test using the

3D industrial camera (ZEISS ARAMIS 3D, Carl Zeiss IQS GmbH, Oberkochen, Germany) was evaluated with ZEISS INSPECT software to measure the strain.[53]

The strain measurements along the *y*-axis including the regions where the maximum strain occurred are highlighted for both the structural electrolyte and structural electrode as shown in Fig. 10e and f, respectively. The calculated Young's moduli of the SPEs and multifunctional composites are given in Table 1. To ensure repeatability, six samples were tested, and the statistical analysis is shown in Fig. S15 (ESI†). The force–displacement curves for all the tested samples are shown in Fig. S16 (ESI†).

The thermal stability of the SPE (PEO–PVP–InAsNW–$NaPF_6$) and the structural electrolyte (GF_PEO–PVP–InAsNW–$NaPF_6$) was analyzed by heating the samples at 160 °C for 15 minutes, the SPE melted away after 10 minutes, while the structural electrolyte retained its shape as shown in Fig. S17 (ESI†). This shows the glass fibers' ability to absorb the melted electrolyte through capillary action ensuring its shape stability.

Structural battery performance and characterization

The structural cell CF‖GF_PEO–PVP–InAsNW–$NaPF_6$‖Na was fabricated in the 2032 coin-cell configuration as detailed in Section 2. To assess the performance, it was cycled at a constant 0.1C rate and charged till it reached 3.6 V and further charged in constant voltage mode for a short duration, and then the cell was discharged until it reached 1.4 V as shown in Fig. 11a. In the first cycle, the discharge capacity reached a value of 12.3 Ah kg^{-1} and the charge capacity was 7.4 Ah kg^{-1}. In the second cycle, the discharge capacity was changed to 7.3 Ah kg^{-1}, indicating that the solid–electrolyte interphase (SEI) layer had formed, and the coulombic efficiency had improved when compared with the first cycle.[54] The cell was analyzed for rate capability by cycling the cell at different C-rates as shown in Fig. 11b, the nominal voltage during discharge was 2.4 V. The cell charge and discharge capacities for different C-rates remained constant during cycling. The typical energy density of the structural cell at 0.1C rate based on the aerial weight of carbon fibers was estimated to be 17.5 Wh kg^{-1}. The cell showed energy densities of 9.6 Wh kg^{-1} at 0.6C rate, 5.8 Wh kg^{-1} at 0.8C rate and 2.4 Wh kg^{-1} at 1.5C rate. The low energy density at high C-rates could be due to internal losses, a lack of the presence of active materials and can also be due to the type of carbon fibers used in the present study. The obtained energy density values typically fall in the range of DOI III structural battery architectures reported in the past.[13,55–60] The plot showing the performance comparison of structural batteries with various degrees of integration (DOI) is shown in Fig. S18 (ESI†). At the time of reporting this work, the current DOI level III and IV structural battery approaches fall in the range between 1 and 50 Wh kg^{-1}, and the future research trend is on improving the energy density of higher DOI structural batteries.

Table 1 Summary of tensile strength and Young's moduli of electrolytes and multifunctional composites

Electrolytes/composites	Tensile strength (MPa)	Youngs modulus (GPa)
PEO–PVP–$NaPF_6$	4.5	0.192
PEO–PVP–InAsNW–$NaPF_6$	6.1	0.43
GF_PEO–PVP–InAsNW–$NaPF_6$	76.5	4.4
CF|GF_PEO–PVP–InAsNW–$NaPF_6$	171.5	7.9

Table S3 (ESI†) summarizes the energy densities of DOI III type structural batteries, and Fig. S19 (ESI†) compares the energy densities of the previous approaches for sodium-ion based structural cells with the present work. The plot of energy density *vs.* elastic modulus of various reported DOI III type structural batteries in the literature including the current work is shown in Fig. S20 (ESI†). To further analyze the long-term cycling stability, the cell was galvanostatically charged and discharged at 0.8C rate, and the cycling curves until 400 cycles are shown in Fig. 11c. The cell initially had a coulombic efficiency of 62% for the first cycle but exhibited a high coulombic efficiency from cycle 5 onwards and that was maintained throughout 600 cycles, as shown in Fig. 11d. The discharge energy density plot is also shown in Fig. 11d, indicating that the cell was able to retain 80% of its initial capacity until the end of 280 cycles and approximately 50% of its initial capacity at the end of 600 cycles.

This high cycling stability can be attributed to both the incorporation of InAs NW fillers, which showed the ability to delay sodium dendrite formation, and to the stable SEI layer formation during the first cycle, which prevented short circuiting of the cell with localized sodium plating. The capacity degradation of the cell is evident from Fig. 11d and it is inevitable due to sodium dendrite formation, and it is also reflected in the EIS plot in the high-frequency regions as shown in Fig. 11e.[32,61,62] It shows the increase in interfacial resistance (R_{if}) from the initial 4.5 kΩ before cycling to nearly 8.5 kΩ (represented by the diameter of the semicircle in the Nyquist plot) at the end of the 600th cycle. Fig. 11f and Fig. S21 (ESI†) show the SEM image of the CF electrode and Na electrode after cycling, respectively. The fabricated multifunctional matrix material (structural electrolyte) in this work displayed considerable cycling stability, ionic conductivity and tensile strength, and the structural electrode showed high tensile strength which are essential for structural battery design. The good cycling stability of the structural cell CF‖GF_PEO–PVP–InAsNW–$NaPF_6$‖Na demonstrated the Na–ion intercalation capabilities with the intermediate modulus CF electrode. Future work for the construction of full structural batteries requires the replacement of the Na metal with suitable sodium rich active material coated CFs functioning as the cathode and CFs laminated with the structural electrolyte as the anode (CF‖GF_PEO–PVP–InAsNW–$NaPF_6$‖CF (cathode)). The CFs in a full structural battery also act as current collectors and the resin infused full structural battery is expected to have exceptional tensile strength suitable for various structural energy storage applications. The multifunctional composite of DOI level III presented in this paper investigated a single cell stack and the full structural battery will comprise of many such cell stacks which are expected to further improve the overall energy density of the material. Also, the performance of the battery function is expected to scale up with the size such as an aircraft structure, which could help in optimizing the energy system design of the aircraft. Some proposed optimization plans in future work

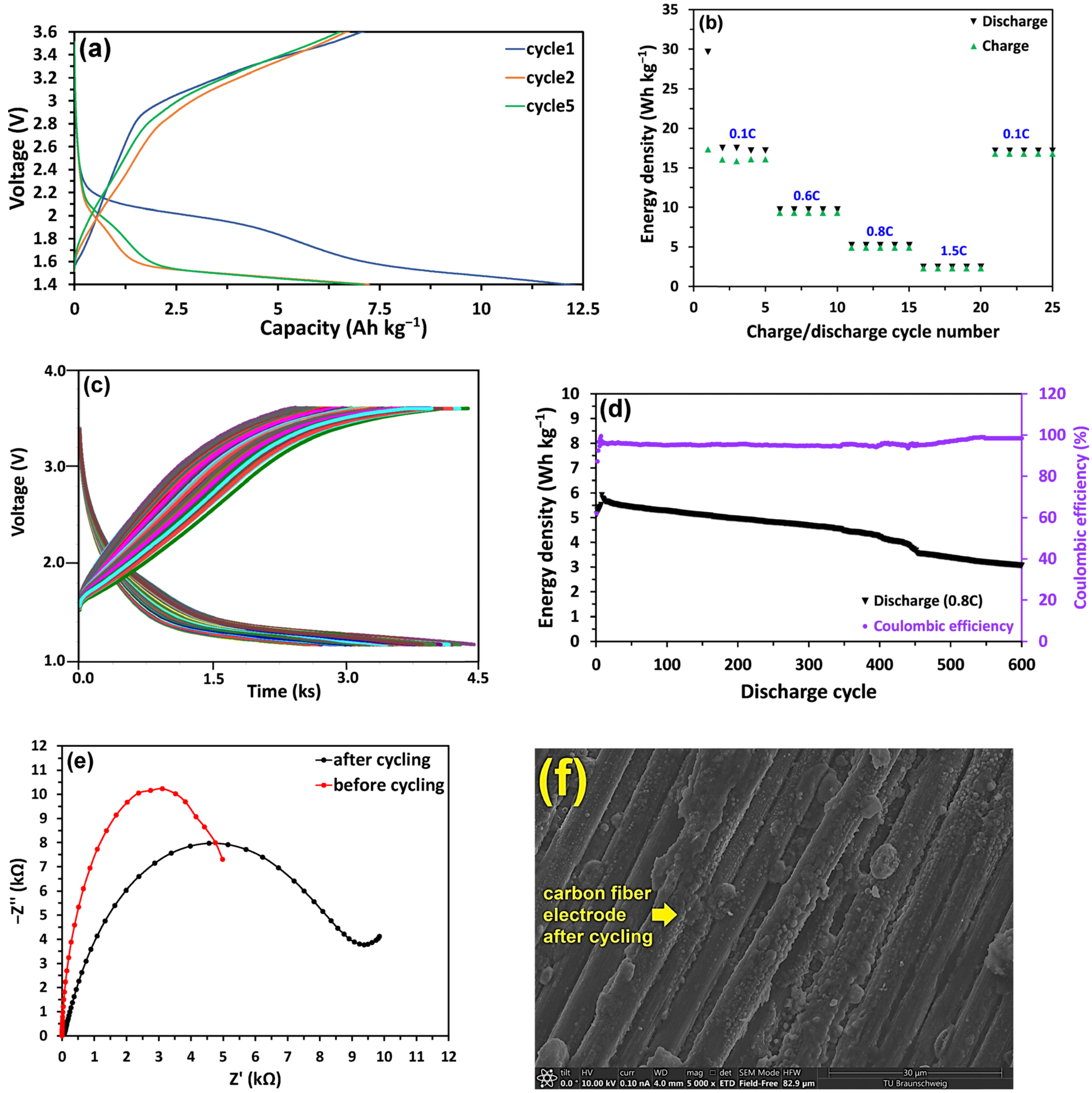

Fig. 11 Performance of the structural cell CF‖PEO–PVP–InAsNW–NaPF$_6$‖Na: (a) voltage profiles of the cell at 0.1C rate. (b) Energy density of the cell at different C rates. (c) Charge–discharge profiles of the cell for the first 400 cycles at 0.8C rate. (d) Long term cycling tests showing energy density and coulombic efficiency *vs.* cycle number for the 0.8C rate. (e) EIS of the cell before and after cycling. (f) SEM image of the carbon fiber electrode after cycling.

are to investigate glass fibers with less aerial weight or to find a replacement to glass fibers to optimize and reduce the contact resistance, chemical treatment of carbon fibers to remove the binders to further improve the energy storage capacity, chemical coating of CFs with 2D nanomaterials to improve the carbon fiber surface properties favorable for more energy storage and improved fabrication techniques to further boost the cell performance.

Conclusions

In this work, we fabricated and characterized novel multifunction composites for sodium-ion based structural battery applications. The structural electrolyte was based on a PEO–PVP polymer blend matrix incorporated with InAs nanowires and was fabricated using glass fiber reinforcements. It showed a high tensile strength of 76.5 MPa and ionic conductivity of 1.7×10^{-4} S cm^{-1} at 70 °C, with an electrochemical stability window of 0 to 3.7 V. The structural electrode was fabricated by laminating the prepared structural electrolyte with intermediate modulus carbon fibers, and it showed a high tensile strength of 171.5 MPa. The structural cell CF‖GF_PEO–PVP–InAsNW–NaPF$_6$‖Na was fabricated with the prepared structural electrode as the cathode and sodium metal as the anode material, and it provided a typical energy density of 17.5 Wh kg^{-1} at 0.1C rate. The cell was tested for its long term cycling stability by charging–discharging at 0.8C rate and it performed 600 cycles, maintained high coulombic efficiency and exhibited the ability to retain 80% of its capacity at the end of 280 cycles. The preliminary work showed that incorporation of InAs nanofillers into the polymer blend matrix enhanced both the tensile strength and ionic conductivity of the structural electrolyte and boosted the performance of the structural cell by suppressing sodium dendrite formation. The glass fiber reinforcements greatly improved the tensile strength of the multifunctional composites and ensured shape stability of the structural electrolyte at high temperatures. The structural electrodes with intermediate modulus carbon fibers demonstrated sodium-ion intercalation capabilities. The fabricated multifunctional composites displayed both electrochemical and mechanical characteristics essential for designing sodium-ion structural batteries.

Author contributions

Vasan Iyer: conceptualization, methodology, formal analysis, investigation, data curation, visualization, software, and writing – original draft. Sandeep Kumar: resources, validation, visualization, and writing – review and editing. Håkan Pettersson: resources, validation, and writing – review and editing. Jan Petersen: resources and writing – review and editing. Sebastian Geier: resources, validation, supervision, and writing – review and editing. Peter Wierach: project administration, funding acquisition, resources, and supervision. All authors have read and agreed to the published version of the manuscript.

Conflicts of interest

The authors declare no conflicts of interest.

Data availability

The authors confirm that the data supporting the findings of this study are available within the article and/or its ESI.†

Acknowledgements

We would like to acknowledge the funding by the Deutsche Forschungsgemeinschaft (DFG, German Research Foundation) under Germany's Excellence Strategy – EXC 2163/1-Sustainable and Energy Efficient Aviation – Project-ID 390881007. Furthermore, we acknowledge support by the Open Access Publication Funds of the Technische Universität Braunschweig and German Aerospace Center (DLR).

References

1 European Commission, The European Green Deal, https://europa.eu/!DG37Qm, accessed: January 2025.
2 Sustainable and Energy-Efficient Aviation (SE2A) Symposium on Climate and Sustainability, Braunschweig, Germany, October 2019, https://www.tu-braunschweig.de/en/se2a, accessed: January 2025.
3 European Commission. Clean Sky Benefits, https://www.clean-aviation.eu/benefits-for-cleaner-greener-healthier-skies, accessed: January, 2025.
4 European Commission, Flightpath 2050, https://data.europa.eu/doi/10.2777/15458, accessed: January 2025.
5 NASA, NASA Aeronautics – Strategic Implementation Plan—2019 Update, https://www.nasa.gov/sites/default/files/atoms/files/sip-2019-v7-web.pdf, accessed: January 2025.
6 https://www.businessinsider.com/how-the-electric-ce-liner-plane-works-2012-9, accessed: January 2025.
7 Tesla Battery Pack Architecture. https://futurism.com/take-an-in-depth-look-at-the-tesla-model-3s-newbattery-pack-architecture, accessed: January 2025.
8 E. D. Wetzel, *AMPTIAC Q.*, 2004, **8**, 91–95.
9 T. J. Adam, G. Liao, J. Petersen, S. Geier, B. Finke, P. Wierach, A. Kwade and M. Wiedemann, *Energies*, 2018, **11**, 335.
10 J. P. Thomas and M. A. Qidwai, *Acta Mater.*, 2004, **52**, 2155–2164.
11 T. Pereira, Z. Guo, S. Nieh, J. Arias and T. Hahn, *Compos. Sci. Technol.*, 2008, **68**, 1935–1941.
12 J. Petersen, A. Kube, S. Geier and P. Wierach, *Sensors*, 2022, **22**, 6932.
13 P. Liu, E. Sherman and A. Jacobsen, *J. Power Sources*, 2009, **189**, 646.
14 S. Leijonmarck, T. Carlson, G. Lindbergh, E. S. Asp, H. Maples and A. Bismarck, *Compos. Sci. Technol.*, 2013, 149–157.
15 Y. Yu, B. Zhang, M. Feng, G. Qi, F. Tian, Q. Feng, J. Yang and S. Wang, *Compos. Sci. Technol.*, 2017, **147**, 62–70.
16 Sedan Automotive – Designed by Freepik. https://www.freepik.com/free-vector/blue-sedan-automotive-design_16269712.htm, accessed: January 2025.
17 L. E. Asp, M. Johansson, M. G. Lindbergh, J. Xu and D. Zenkert, *Funct. Compos. Struct.*, 2019, **1**, 042001.
18 F. Danzi, R. M. Salgado, J. E. Oliveira, A. Arteiro, P. P. Camanho and M. H. Braga, *Molecules*, 2021, **26**, 2203.
19 H. Kühnelt, A. Beutl, F. Mastropierro, F. Laurin, S. Willrodt, A. Bismarck, M. Guida and F. Romano, *Aerospace*, 2022, **9**, 7.
20 J. K. Lee, K. W. An, J. B. Ju, B. W. Cho, W. I. Cho, D. Park and K. S. Yun, *Carbon*, 2001, **39**, 1299–1305.
21 M. H. Kjell, E. Jacques, D. Zenkert, M. Behm and G. Lindbergh, *J. Electrochem. Soc.*, 2011, **158**, A1455–A1460.
22 W. Johannisson, N. Ihrner, D. Zenkert, M. Johansson, D. Carlsted, L. E. Asp and F. Sieland, *Compos. Sci. Technol.*, 2018, **168**, 81–87.
23 S. Geier, J. Petersen, V. Iyer and P. Wierach, in Challenges of integrating supercapacitors into structures for space qualification, Proceedings of the 16th European Conference on Spacecraft Structures, Materials and Environmental Testing (ECSSMET 2021), Braunschweig, Germany, 2021.
24 E. Jacques, M. H. Kjell, D. Zenkert, G. Lindbergh, M. Behm and M. Willgert, *Compos. Sci. Technol.*, 2012, **72**, 792–798.
25 J. F. Snyder, R. H. Carter and E. D. Wetzel, Integrating Structure with Power in Battery Materials. In Proceedings of

the 2004 Army Science Conference, Orlando, Florida, USA, 2004.

26 L. M. Schneider, N. Ihrner, D. Zenkert and M. Johansson, *ACS Appl. Energy Mater.*, 2019, **2**, 4362–4369.

27 D. A. Stevens and J. R. Dahn, *J. Electrochem. Soc.*, 2001, **148**(8), A803–A811.

28 P. Thomas and D. Billaud, *Electrochim. Acta*, 2001, **46**, 3359–3366.

29 B. Zhang, C. Matei Ghimbeu, C. Laberty, C. Vix-Guterl and J. M. Tarascon, *Adv. Energy Mater.*, 2016, **6**(1), 1.

30 M. H. Kjell, T. G. Zavalis, M. Behm and G. Lindbergh, *J. Electrochem. Soc.*, 2013, **160**, A1473–A1481.

31 G. Fredi, S. Jeschke, A. Boulaoued, J. Wallenstein, M. Rashidi, F. Liu, R. Harnden, D. Zenkert, J. Hagberg, G. Lindbergh, P. Johansson, L. Stievano and L. E. Asp, *Multifunct. Mater.*, 2018, **1**, 015003.

32 G. Dong, Y. Mao, G. Yang, Y. Li, S. Song, C. Xu, P. Huang, N. Hu and S. Fu, *ACS Appl. Energy Mater.*, 2021, **4**(4), 4038–4049.

33 Q. Zhao, S. Stalin, C. Z. Zhao and L. A. Archer, *Nat. Rev. Mater.*, 2020, **5**, 229–252.

34 E. Goikolea, V. Palomares, S. Wang, I. R. de Larramendi, X. Guo, G. Wang and T. Rojo, *Adv. Energy Mater.*, 2020, **10**, 2002055.

35 D. E. Fenton, J. M. Parker and P. V. Wright, *Polymer*, 1973, **14**, 589.

36 M. Armand, J.-M. Chabagno and M. J. Duclot, in *Proceedings of Fast Ion Transport in Solids: Electrodes and Electrolytes*, ed. P. Vashishta, J. N. Mundy and G. K. Shenoy, Elsevier, Lake Geneva, WI, USA, 1979, vol. 5.

37 Q. L. Ma, M. Guin, S. Naqash, C. L. Tsai, F. Tietz and O. Guillon, *Chem. Mater.*, 2016, **28**, 4821–4828.

38 J. J. Kim, K. Yoon, I. Park and K. Kang, *Small Methods*, 2017, **1**, 1700219.

39 O. Borodin and G. D. Smith, *Macromolecules*, 2006, **39**(4), 1620–1629.

40 V. Iyer, J. Petersen, S. Geier and P. Wierach, *ACS Appl. Energy Mater.*, 2024, **7**, 3968–3982.

41 V. Iyer, J. Petersen, S. Geier and P. Wierach, *Polymers*, 2024, **16**, 2806.

42 H. Feng, Z. Feng and L. Shen, *Polymer*, 1993, **34**(12), 2516–2519.

43 K. K. Kumar, M. Ravi, Y. Pavani, S. Bhavani, A. K. Sharma and V. N. Rao, *Phys B: Cond. Matter.*, 2011, **406**(9), 1706–1712.

44 A. Arya and A. L. Sharma, *J. Solid State Electrochem.*, 2018, **22**, 2725–2745.

45 W. Liu, S. Lee, D. Lin, F. Shi, S. Wang, A. D. Sendek and Y. Cui, *Nat. Energy*, 2017, **2**, 17035.

46 C. Devi, R. Singhal, K. da Silva, W. Paschoal Jr, H. Pettersson and S. Kumar, *Nanotechnology*, 2020, **31**(23), 235709.

47 J. Evans, C. A. Vincent and P. G. Bruce, *Polymer*, 1987, **28**, 2324–2328.

48 ASTM-D638 Standards, **https://www.zwickroell.com/industries/plastics/thermoplastics-and-thermosetting-molding-materials/tensile-properties-astm-d638**, accessed: January 2025.

49 C. Devi, J. Gellanki, H. Pettersson and S. Kumar, *Sci. Rep.*, 2021, **11**, 20180.

50 D. Li, L. Chen, T. Wang and L. Z. Fan, *ACS Appl. Mater. Interfaces*, 2018, **10**, 7069–7078.

51 B. Lee, E. Paek, D. Mitlin and S. W. Lee, Sodium Metal Anodes: Emerging Solutions to Dendrite Growth, *Chem. Rev.*, 2019, **119**(8), 5416–5460.

52 S. Komaba, T. Ishikawa, N. Yabuuchi, W. Murata, A. Ito and Y. Ohsawa, *ACS Appl. Mater. Interfaces*, 2011, **3**, 4165–4168.

53 ZEISS INSPECT software **https://www.zeiss.de/messtechnik/software/zeiss-inspect.html**, accessed: January 2025.

54 M. Feng, S. Wang, Y. Yu, Q. Feng, J. Yang and B. Zhang, *Appl. Surf. Sci.*, 2017, **392**, 27–35.

55 C. Meng, N. Muralidharan, E. Teblum, K. E. Moyer, G. D. Nessim and C. L. Pint, *Nano Lett.*, 2018, **18**, 7761–7768.

56 A. Thakur and X. Dong, *Manuf. Lett.*, 2020, **24**, 1–5.

57 K. Moyer, C. Meng, B. Marshall, O. Assal, J. Eaves, D. Perez, R. Karkkainen, L. Roberson and C. L. Pint, *Energy Stor. Mater.*, 2020, **24**, 676–681.

58 L. E. Asp, K. Bouton, D. Carlstedt, S. Duan, R. Harnden, W. Johannisson, M. Johansen, M. K. G. Johansson, G. Lindbergh, F. Liu, K. Peuvot, L. M. Schneider, J. Xu and D. Zenkert, *Adv. Energy Sustainability Res.*, 2021, **2**, 2000093.

59 M. S. Siraj, S. Tasneem, D. Carlstedt, S. Duan, M. Johansen, C. Larsson, J. Xu, F. Liu, F. Edgren and L. E. Asp, *Adv. Energy Sustainability Res.*, 2023, **4**, 2300109.

60 B. J. Hopkins, J. W. Long, D. R. Rolison and J. F. Parker, *Joule*, 2020, **4**, 2240–2243.

61 Q. Zhang, Y. Lu, W. Guo, Y. Shao, L. Liu, J. Lu, X. Rong, X. Han, H. Li, L. Chen and Y. Hu, *Energy Mater Adv.*, 2021, 9870879.

62 S. Sukumaran, R. Chater, S. Fearn, G. Cooke, N. Smith and S. Skinner, *EES Bat.*, 2021, DOI: **10.1039/D5EB00071H**.